Anharmonic phonon-polariton dynamics in ferroelectric $LiNbO_3$ studied with single-shot pump-probe imaging spectroscopy

T. Kuribayashi, T. Motoyama, Y. Arashida, I. Katayama, and J. Takeda

Citation: Journal of Applied Physics **123**, 174103 (2018); doi: 10.1063/1.5021379
View online: https://doi.org/10.1063/1.5021379
View Table of Contents: http://aip.scitation.org/toc/jap/123/17
Published by the American Institute of Physics

Anharmonic phonon-polariton dynamics in ferroelectric $LiNbO_3$ studied with single-shot pump-probe imaging spectroscopy

T. Kuribayashi, T. Motoyama, Y. Arashida, I. Katayama, and J. Takeda[a)]
Department of Physics, Faculty of Engineering, Yokohama National University, Yokohama 240-8501, Japan

(Received 4 January 2018; accepted 20 April 2018; published online 7 May 2018)

We demonstrate that single-shot pump-probe imaging spectroscopy with an echelon mirror enables us to disclose the ferroelectric phonon-polariton dynamics across a wide temperature range from 10 K to 375 K while avoiding the photorefractive effects that appear prominently at low temperatures. The E-mode phonon-polaritons corresponding to the two transverse optical modes, TO_1 and TO_3, up to ~7 THz were induced in $LiNbO_3$ through an impulsive stimulated Raman scattering process. Subsequently, using single-shot pump-probe imaging spectroscopy over a minimal cumulative time, we successfully visualized the phonon-polariton dynamics in time-wavelength space even at low temperatures. We found that the phase-matching condition significantly affected the observed temperature-dependent phonon-polariton frequency shift. The anharmonicity of the TO_1 and TO_3 modes was then evaluated based on an anharmonic model involving higher-order interactions with acoustic phonons while eliminating the influence of the frequency shift due to the phase-matching condition. The observed wavenumber-dependent damping rate was analyzed by considering the bilinear coupling of the TO_1 or TO_3 modes with the thermally activated relaxation mode. We found that the phonon-polariton with a higher frequency and wavenumber had a higher damping rate at high temperatures because of its frequent interaction with the thermally activated relaxation mode and acoustic phonons. The TO_3 mode displayed greater bilinear coupling than the TO_1 mode, which may also have contributed to the observed high damping rate. Thus, using our unique single-shot spectroscopy technique, we could reveal the overall anharmonic characteristics of the E-mode phonon-polaritons arising from both the acoustic phonons and the relaxation mode. *Published by AIP Publishing.*
https://doi.org/10.1063/1.5021379

I. INTRODUCTION

Ferroelectric materials offer a wide range of useful physical properties: high permittivities, high piezoelectric effects, and strong optical nonlinearities.[1] Among these materials, $LiNbO_3$ (LN) is a typical ferroelectric material whose crystal structure belongs to the space group of *R3c* with $4A_1 + 5A_2 + 9E$ optical modes.[2] Because of its large nonlinear susceptibility, LN has been widely used in various types of nonlinear optical applications such as harmonic generation, electro-optic modulation, and terahertz (THz) generation. Recent research has produced intense THz electric fields at more than 1 MV/cm using an LN prism with a tilted-pulse-front configuration.[3] A cryogenically cooled LN crystal can further enhance the THz-generation efficiency.[4–6] To obtain high power THz waves with the desirable bandwidth, the specific design of LN crystals such as MgO-doped LN ridged waveguide[7] and transversely patterned periodically poled LN (PPLN)[8,9] has also been demonstrated. These intense THz electric fields can introduce intriguing nonlinear properties in various materials such as THz-field-induced photovoltaic effects, phase transitions, electron tunneling, and anharmonic vibrations of ferroelectric soft modes.[10–14] Very recently, using ultrashort mid-infrared laser pulses to drive the atoms far from their equilibrium positions in LN crystals, strong-field-induced higher-order transverse optical phonons have been generated over several tens of THz frequencies.[15] Therefore, performing observations of light-induced lattice vibrations located in the THz-frequency region (so-called phonon-polaritons) over a wide range of temperatures remains an important task. Although the dynamic behaviors of ferroelectric phonon-polaritons have been studied using ultrafast measurements,[16–18] most of these experiments were conducted at room temperature. Obtaining measurements at temperatures lower than ~170 K was quite difficult because of the long-lived photorefractive effects.[19] Even though these photorefractive effects are useful for holographic storage applications,[20–22] they disturb the low-temperature optical measurements that are indispensable for fully understanding the phonon-polariton dynamics.

Recently, we have developed a method that uses single-shot time-frequency two-dimensional (2D) imaging spectroscopy with an echelon mirror to visualize the photoinduced irreversible reactions of materials.[23–25] This technique enabled clear observations of the ultrafast amorphization of chalcogenide alloy films[26] and the THz dielectric responses of a Si plate under the existence of long-lived carriers.[27] In this study, we demonstrate that our technique for performing single-shot imaging spectroscopy has the capability of disclosing ferroelectric phonon-polariton dynamics across a wide temperature range from 10 K to 375 K while eluding the persistent photorefractive effects that appear remarkably at low temperatures. Using ordinary and extraordinary light components with a pulse duration of 40 fs, E-mode phonon-polaritons corresponding to

a)Author to whom correspondence should be addressed: jun@ynu.ac.jp

the TO_1 (~3 THz and ~4 THz) and TO_3 (~7 THz) transverse optical modes with different wavenumbers were induced in an LN crystal through an impulsive stimulated Raman scattering (ISRS) process. Subsequently, the phonon-polariton dynamics was visualized readily in time-wavelength space using single-shot pump-probe imaging spectroscopy, even at low temperatures. In order to unveil the observed phonon-polariton dynamics, we considered not only the temperature-dependent phase-matching condition to generate the E-mode phonon-polaritons but also two anharmonic interactions: the higher-order interaction with acoustic phonons[28,29] and the bilinear coupling with the thermally activated relaxation mode.[17,18] The former served for a discussion of each phonon-polariton softening with increasing temperature. On the other hand, the latter was mainly used to explain the temperature and wavenumber dependences of the damping rate. We show that these analyses are needed to unveil the overall anharmonic E-mode phonon-polariton dynamics in LN.

II. EXPERIMENTAL SETUP

We used a nominally pure *x*-cut LN single crystal with a thickness of 2 mm (Shanghai Daheng Optics and Fine Mechanics) as a sample, which was grown by the Czochralski method. The LN crystal typically contained 5 mass ppm or less of several elements such as Si, Ca, Na, Fe, Mg, Sb, and Ta. Note that the nominally pure LN crystal is suitable for our experiments because our purpose is to unveil the anharmonic phonon-polariton dynamics across a wide temperature range while avoiding the photorefractive effects that commonly appeared in ferroelectric crystals. Figure 1 shows a schematic diagram of our experimental setup for single-shot pump-probe imaging spectroscopy with an echelon mirror. The echelon mirror consisted of 500 steps with a step-height of 5 μm and a step-width of 20 μm, yielding an overall delay time of ~17 ps

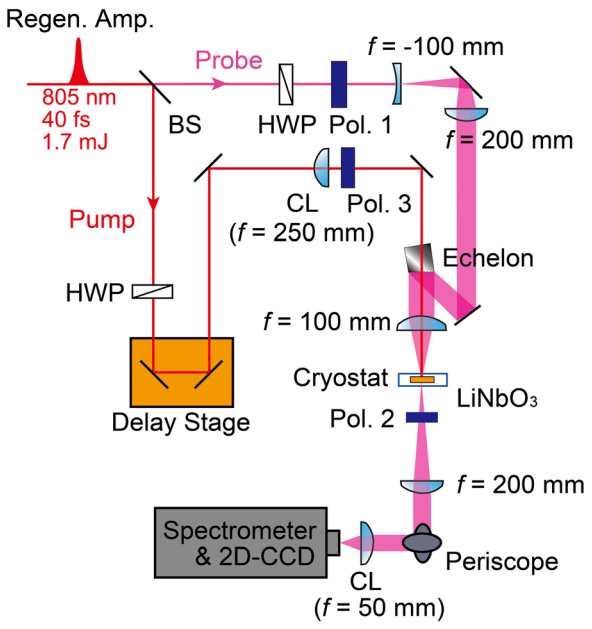

FIG. 1. Schematic of the experimental setup for single-shot real-time pump-probe imaging spectroscopy with an echelon mirror. BS, beam splitter; CL, cylindrical lens; HWP, half-wave plate; and Pol, polarizer.

with a time step of ~34 fs.[23] The light source was a Ti:Sapphire regenerative amplifier with a center wavelength of 805 nm, a pulse duration of 40 fs, and a repetition of 1 kHz. The output of the amplifier was divided into two beams: pump (70%) and probe (30%) beams. Using a combination of a half-wave plate (HWP) and a polarizer (Pol. 1 or Pol. 3), both the pump and probe beams were sufficiently attenuated to prevent laser-induced damages of the LN crystal; the pump intensity was kept at ~3 mJ/cm^2, while the probe intensity was 500 times smaller than the pump intensity. These values were much smaller than the damage threshold (~0.35 J/cm^2) of undoped LN crystals under the irradiation of femtosecond laser pulses with 40-fs pulse duration.[30,31] We also confirmed that undesirable nonlinear phenomena such as multi-photon absorption and white light continuum were not observed in the LN crystal. The probe beam was diffracted by the echelon mirror, which was placed between a pair of crossed polarizers (Pol. 1 and Pol. 2). The probe beam was then focused on the LN single crystal together with the pump beam whose beam size (typically 1 mm) covered the entire probe beam area.[23] The sample was mounted in a temperature-controlled He-flow cryostat. After passing through the sample, the probe beam was imaged onto an entrance slit of a spectrometer coupled with a 2D charge-coupled device (CCD) detector (1024 × 1024 pixels) to obtain a time-wavelength 2D image of the phonon-polariton dynamics at various temperatures. The typical exposure time of the CCD detector was only 0.1 s (representing 100 cumulative laser shots) in our single-shot imaging spectroscopy, which allowed us to implement real measurements to reveal phonon-polariton dynamics while avoiding the photorefractive effects that persist at low temperatures. The sample position was shifted slightly for each measurement to further reduce the residual photorefractive effects. The polarization of the pump pulse was set to 45° (Pol. 3) against the *c*-axis of the LN crystal, while the probe beam's polarization was oriented along the ordinary light direction. The dynamics of the E-mode phonon-polaritons up to ~7 THz induced through the ISRS process was visualized in the specific time-wavelength space (780–830 nm in wavelength) using this optical Kerr gate apparatus with heterodyne detection.[17,32] This scheme allows us to sufficiently eliminate the undesirable nonlinear phenomena, while both the forward- and backward-propagating TO_1 modes, and the backward-propagating TO_3 mode in which the phase-matching conditions were satisfied, were observed. We note that the phonon-polaritons with frequencies higher than ~7.5 THz may not have been induced through the ISRS process because of the limitation of the pulse duration.

III. RESULTS AND DISCUSSION

A. E-mode phonon-polariton dynamics in a wide temperature range from 10 K to 375 K

First, we determined how the persistent photorefractive effects prevent the observation of the phonon-polariton dynamics. Figure 2 shows the time-wavelength 2D images of the ultrafast responses in LN during pump-pulse irradiations at 77 K. After the pump pulse had been irradiated for 1 s, ultrafast responses were still observed in time-wavelength

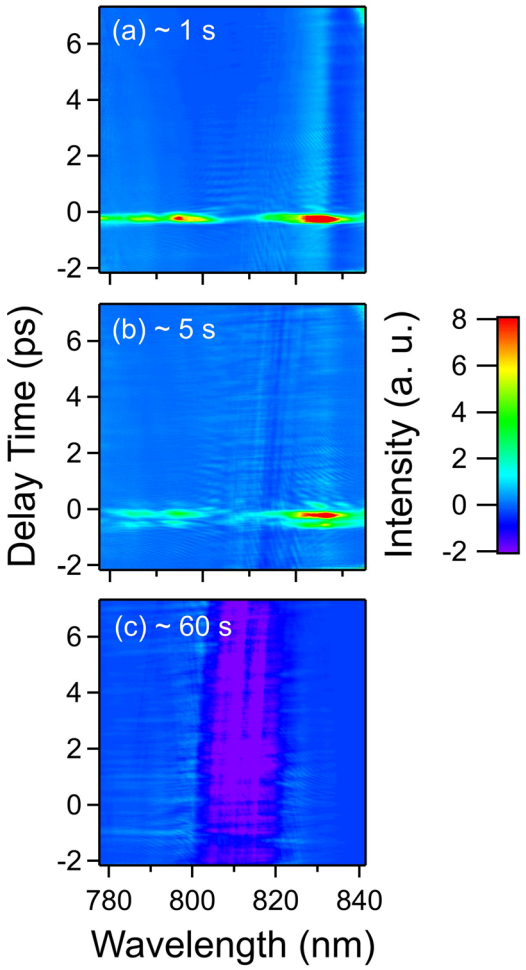

FIG. 2. Time-wavelength 2D images of ultrafast responses in LN at 77 K after irradiations of (a) ~1 s, (b) ~5 s, and (c) ~60 s. The 2D images were taken with an exposure time of 0.1 s (100 cumulative shots).

space. However, the 2D image began to collapse after irradiation of ~5 s and became completely distorted after irradiation lasting ~60 s. Therefore, measurements should be completed within 1 s to exclude the photorefractive effects. This result provides a strong indication that conventional pump-probe spectroscopy based on repetitive measurements is not suitable in this context. In contrast, our single-shot pump-probe imaging spectroscopy proved capable of observing real ultrafast responses in the resulting 2D image.

Figure 3(a) shows time-wavelength 2D images of the E-mode phonon-polariton propagations at 10 K, 50 K, and 375 K. Oscillations attributed to the E-mode phonon-polaritons were observed following an instantaneous electric response at $t = 0$ s. As indicated by the dashed ovals in Fig. 3(b), the Fourier-transformed spectra of the oscillatory components reveal the existence of three different phonon-polariton components with frequencies of ~3 THz, ~4 THz, and ~7 THz, respectively. Both the phase-matching condition and dispersion relation of the E-mode phonon-polaritons were examined to elucidate the origin of the three observed components. Under the phase-matching condition, the wavevectors of the backward- and forward-propagating phonon-polaritons, k_- and k_+, are given by[17]

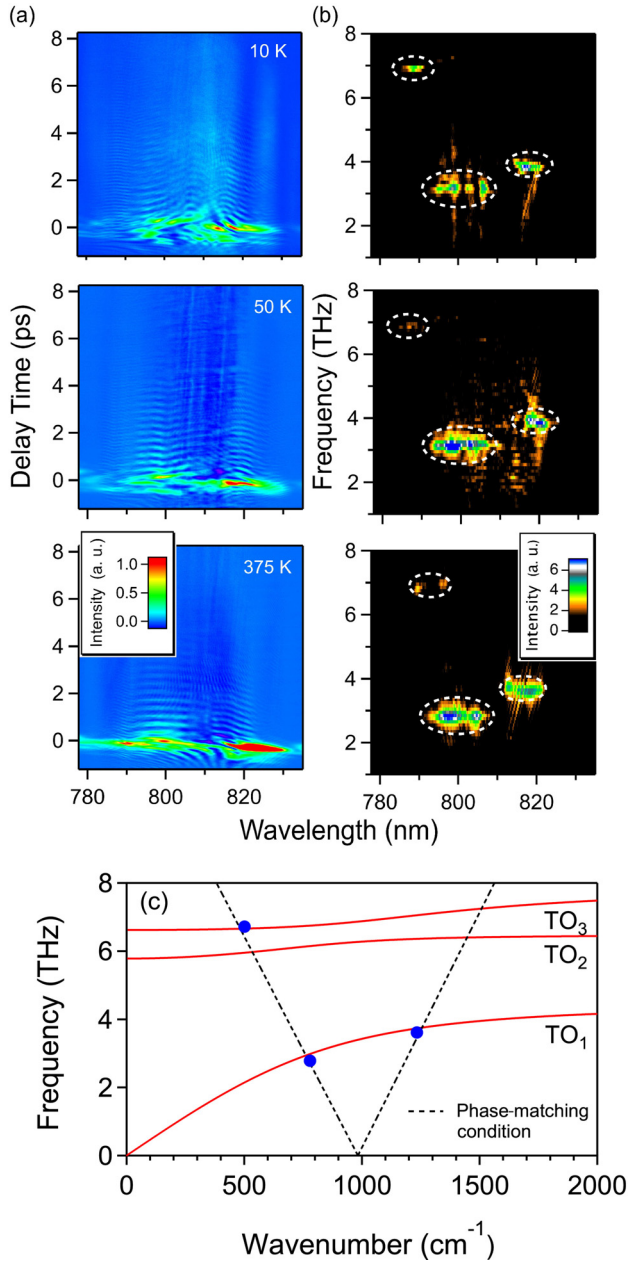

FIG. 3. (a) Time-wavelength 2D images of E-mode phonon-polariton propagations at 10 K, 50 K, and 375 K. (b) Fourier-transformed 2D images of the oscillatory components in (a). Dashed ovals enclose the E-mode phonon-polaritons induced via the ISRS process. The remaining noise came from the interference between the pump and probe pulses. (c) Dispersion relation of the E-mode phonon-polaritons in LN at room temperature. Solid red lines show the three lowest dispersion curves calculated from Eq. (3) with well-known parameters for LN. Solid blue circles show the experimental data. Dashed lines represent the phase-matching conditions calculated from Eqs. (1) and (2).

$$k_- = \frac{n_e}{c}\omega_0 - \frac{n_o}{c}(\omega_0 - \Omega_-) = \frac{(n_e - n_o)}{c}\omega_0 - \frac{n_o}{c}\Omega_-, \quad (1)$$

$$k_+ = \frac{n_o}{c}\omega_0 - \frac{n_e}{c}(\omega_0 - \Omega_+) = \frac{(n_o - n_e)}{c}\omega_0 - \frac{n_e}{c}\Omega_+, \quad (2)$$

where n_e and n_o are the refractive indices of LN for the extraordinary and ordinary lights, respectively, ω_0 is the central frequency of the laser pulse, c is the speed of light, and Ω_- and Ω_+ are the backward- and forward-propagating

phonon-polariton frequencies with different wavenumbers. On the other hand, the dispersion relation is described as

$$k^2 = \frac{\omega^2}{c^2}\left(\varepsilon_{\text{el}} + \sum_i \frac{\varepsilon_{\text{st}_i}\omega_{\text{TO}_i}^2}{\omega_{\text{TO}_i}^2 - \omega^2}\right), \tag{3}$$

where $\varepsilon_{\text{st}_i}$ and ω_{TO_i} are the strength and frequency of the i-th TO phonon, respectively, and ε_{el} (here, 5.0) is the frequency-independent part arising from the vacuum and high-frequency electric process.[2] We could obtain the dispersion relation of the E-mode phonon-polaritons in LN from Eqs. (1)–(3) with well-known physical parameters for LN ($\varepsilon_{\text{st}_1} = 22.0$, $\varepsilon_{\text{st}_2} = 0.8$, and $\varepsilon_{\text{st}_3} = 5.5$; $\omega_{\text{TO}_1} = 148\,\text{cm}^{-1}$, $\omega_{\text{TO}_2} = 216\,\text{cm}^{-1}$, and $\omega_{\text{TO}_3} = 262\,\text{cm}^{-1}$ at room temperature).[2,33,34] Figure 3(c) shows that the three observed components, $\omega_{3\,\text{THz}}$, $\omega_{4\,\text{THz}}$, and $\omega_{7\,\text{THz}}$, are attributed to the backward- and forward-propagating phonon-polaritons at the lowest branch (TO_1 mode) and the backward-propagating one at the third branch (TO_3 mode), respectively. The phonon-polariton at the second branch (TO_2 mode) could not be observed because of its small strength, $\varepsilon_{\text{st}_2} = 0.8$. Figure 3 clearly shows that our single-shot pump-probe imaging spectroscopy has the ultimate capability to accentuate the phonon-polariton dynamics without encountering undesirable photorefractive effects.

B. Anharmonicity of the E-mode phonon-polaritons

Figure 3(b) shows that the three observed phonon-polariton components could be separated fully by the wavelength. Thus, we can reveal each instance of phonon-polariton dynamics in detail. Figure 4 shows the temporal behaviors of the three components observed at different probe wavelengths for various temperatures. These results were obtained by cutting off the 2D images [typically shown in Fig. 3(a)] at a given wavelength. The decay time of each component gradually increased as the temperature decreased. In ferroelectric materials, the phonon-polariton decay profile $f(t)$ can be expressed by a damped harmonic oscillation model with a single exponential decay arising from the relaxation mode[17,18]

$$f(t) = A\exp(-\gamma t)\sin(\omega t + \varphi) + B\exp(-\lambda t), \tag{4}$$

where ω is the phonon-polariton frequency and γ and λ are the damping rates of the phonon-polariton and relaxation modes, respectively. Here, the relaxation mode originates when either of the cations—Nb or Li—undergoes thermally assisted hopping into different local potential energy minima within the unit cell. Then, the damping rate of the relaxation mode can be estimated from the exponential decay of the electric response. After the ultrafast decay attributable to the relaxation mode ($\leq\sim$0.5 ps) had occurred, the observed temporal behaviors were well reproduced by damped harmonic oscillation with two adjustable parameters, ω and γ, as shown by the dark blue curves in Fig. 5. As we will discuss in Sec. III C, the relaxation mode is needed in order to reproduce the high damping rate of γ and its wavenumber dependence.[17,18]

Figure 5 shows the temperature dependence of the phonon-polariton frequencies estimated for the three

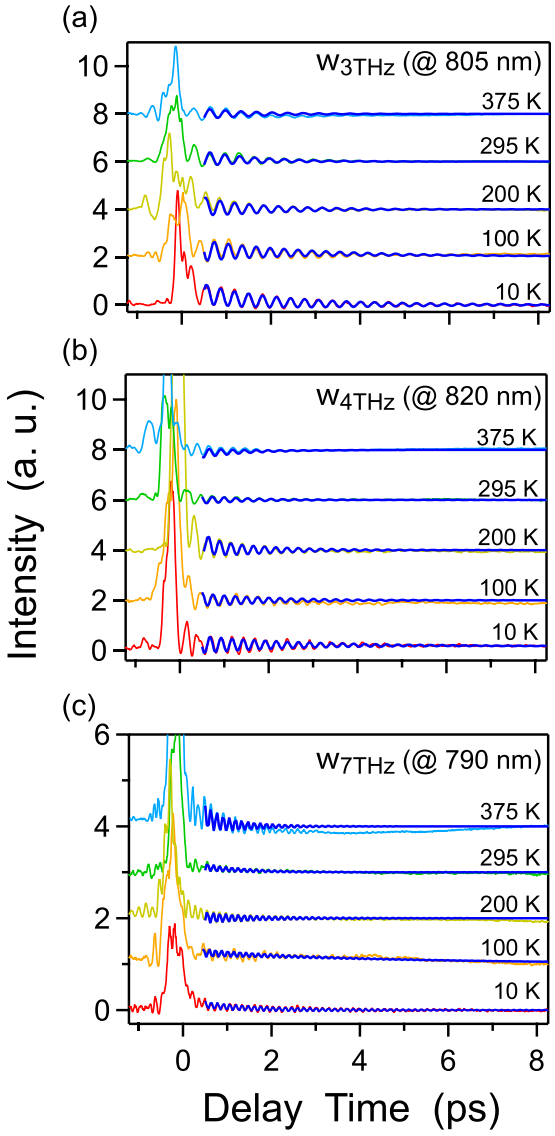

FIG. 4. Time evolutions of three phonon-polariton components $\omega_{3\,\text{THz}}$, $\omega_{4\,\text{THz}}$, and $\omega_{7\,\text{THz}}$ observed at different probe wavelengths between 10 K and 375 K. Solid dark-blue curves show the best-fit lines to the experimental data using Eq. (4).

components: $\omega_{3\,\text{THz}}$, $\omega_{4\,\text{THz}}$, and $\omega_{7\,\text{THz}}$. For all three components, the phonon-polariton frequency exhibits a redshift with increasing temperatures. The components $\omega_{3\,\text{THz}}$ and $\omega_{4\,\text{THz}}$ indicate a redshift of $\sim$0.4 THz, while the component $\omega_{7\,\text{THz}}$ shows a smaller redshift of $\sim$0.1 THz. These values are consistent with those obtained from the previous continuous-wave Raman experiments.[35] The observed redshift can be generally interpreted in terms of the volume expansion and anharmonic interactions with acoustic phonons, such that[36,37]

$$\omega(T) = \omega(0) + \omega(0)K_G T - M_1\left\{1 + 2n\left(\frac{\omega(0)}{2}, T\right)\right\} - M_2\left\{1 + 3n\left(\frac{\omega(0)}{2}, T\right) + 3n^2\left(\frac{\omega(0)}{3}, T\right)\right\}, \tag{5}$$

where $\omega(0)$ is the phonon-polariton frequency at 0 K, K_G, M_1, and M_2 are the coefficients related to the Grüneisen

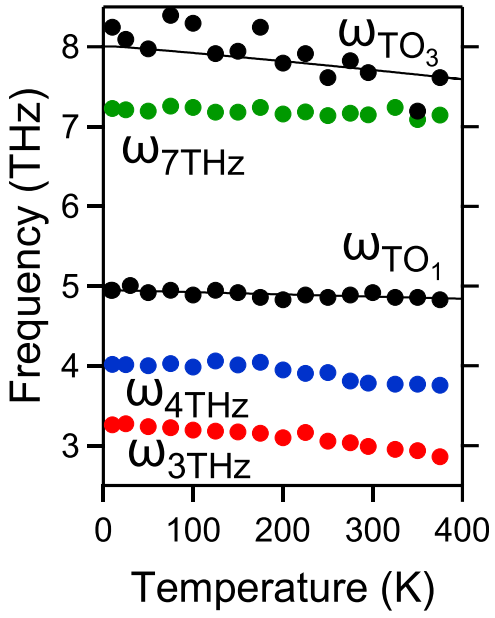

FIG. 5. Temperature dependence of the frequency shift for each phonon-polariton component in LN. The calculated frequency of the TO_1 and TO_3 modes for each temperature is also shown. Solid lines trace the best fits calculated using Eq. (5). The parameter values used here are listed in Table I.

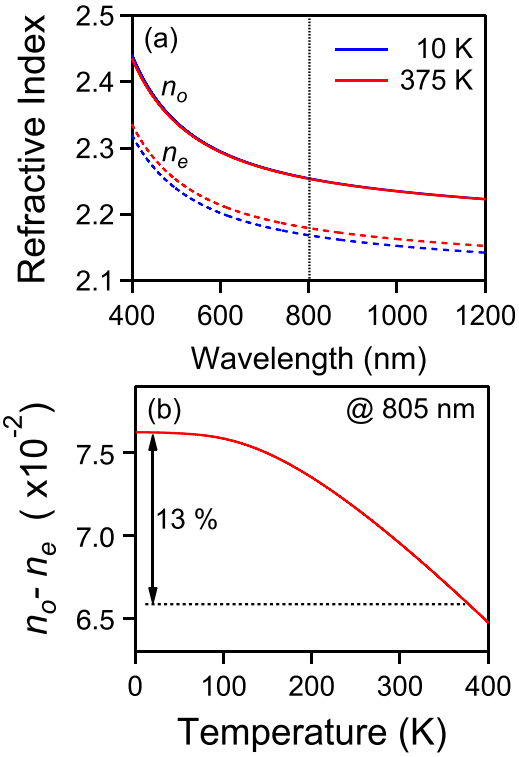

FIG. 6. (a) Refractive indices of LN as a function of the wavelength at 10 K and 375 K. (b) Difference between n_o and n_e at 805 nm as a function of temperature.

parameter, and the anharmonic three- and four-phonon processes, respectively, and $n(\omega, T)$ is the Bose–Einstein population factor.[28,29] Here, a phonon-polariton is assumed to be decomposed into two or three acoustic phonons with the same frequency. The values of K_G for the TO_1 and TO_3 modes have already been estimated to be $4.9 \times 10^{-5}\,K^{-1}$ and $7.0 \times 10^{-6}\,K^{-1}$, respectively.[38] Although the temperature dependence of each frequency shift can be reproduced using Eq. (5) with appropriate parameter values of $\omega(0)$, M_1, and M_2,[39] the anharmonicity of pure transverse optical modes (TO_1 and TO_3 modes) might not be precisely obtained as stated in the following paragraph.

Here, we consider the temperature dependence of the phonon-polariton dispersion relation and the phase-matching condition discussed in Sec. III A. In earlier work, Schlarb and Betzler summarized the experimentally observed refractive indices of LN and derived a generalized fit to various experimental data over a wide temperature and composition range.[40] Following their procedure, in Fig. 6(a), we have depicted the refractive indices n_o and n_e as functions of the wavelength. The values of n_o and n_e are rather insensitive to temperatures between 10 K and 375 K; around the center wavelength of the pump and probe pulses (dashed line), the deviations are only $\sim 5.7 \times 10^{-4}$ and $\sim 1.1 \times 10^{-2}$ for n_o and n_e, respectively. Therefore, the dispersion relation showcased in Fig. 3(c) [or in Eq. (3)] is expected to show only a slight temperature dependence. On the other hand, as shown in Fig. 6(b), the difference $n_o - n_e$ calculated at 805 nm strongly depends on temperature; a $\sim$13% variation takes place in the temperature range from 10 K to 375 K. As seen in Eqs. (1) and (2), this variation may yield significant modulations of the phase-matching conditions. By fitting the experimental data with Eq. (3) (using ω_{TO_1} and ω_{TO_3} as adjustable parameters), we could obtain the temperature dependence of the dispersion relation. In addition, we evaluated the temperature dependence of the phase-matching conditions using Eqs. (1) and (2) with particular values of n_o, n_e, Ω_-, and Ω_+ at a given temperature. Here, we note that the bandwidth of the laser pulses (805 ± 15 nm) was also taken into account to evaluate the upper and lower limits of the phase-matching conditions at different temperatures. Figure 7 shows the upper and lower limits of the phase-matching conditions calculated for the backward- and forward-propagating phonon-polaritons at 10 K (green lines) and 375 K (orange lines) together with the dispersion curves calculated at 10 K, 295 K, and

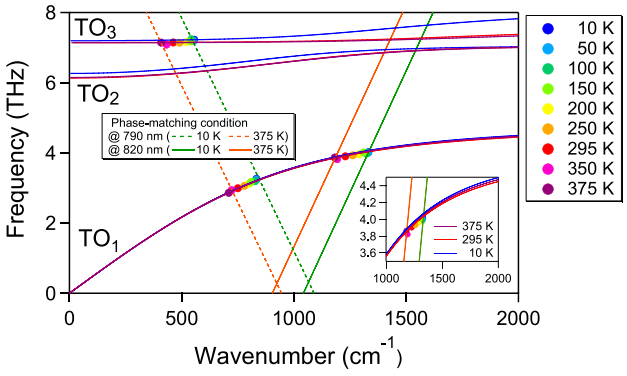

FIG. 7. Dispersion relation of the E-mode phonon-polaritons in LN. The solid curves correspond to the calculated dispersion relations for 10, 295, and 375 K, solid circles to the experimental data at various temperatures, and solid and dashed lines to the phase-matching conditions for the forward- and backward-propagating phonon-polaritons, respectively, calculated at 10 K (green) and 375 K (orange). The inset shows the enlarged phonon-polariton dispersions.

TABLE I. Parameter values for the phonon-polariton components.

Components	$\omega(0)$ (THz)	M_1 (10^{-3} THz)	M_2 (10^{-5} THz)	$\Gamma(0)$ (ps^{-1})	N_1 (10^{-3} ps^{-1})	N_2 (10^{-5} ps^{-1})
TO_1 (ω_{TO_1})	4.95	0.44	0	0.08	3.4	11.0
TO_3 (ω_{TO_3})	8.05	15.7	3.0	…	…	…

375 K (solid curves). With respect to these procedures, the experimental data are in fairly good agreement with the calculated dispersion curves. We note that in response to the temperature-dependent phase-matching conditions, both the frequency and wavenumber of the observed phonon-polaritons decrease with temperature, along with the phonon-polariton dispersions. The calculated dispersion curves show a slight temperature dependence as expected, and thence, we could obtain the temperature-dependent parameter values of ω_{TO_1} and ω_{TO_3}. Thus, using Eq. (5), the anharmonicity of the transverse optical ω_{TO_1} and ω_{TO_3} modes could be calculated as shown by the solid curves in Fig. 5 while eliminating the influence of the temperature-dependent phase-matching conditions. The estimated anharmonic values are listed in Table I.

The results shown in Figs. 5–7 suggest several important conclusions. The anharmonic interactions with acoustic phonons induce phonon-polariton softening in the THz regions, as was previously reported in continuous-wave Raman experiments.[29,36,39] This anharmonicity may introduce slight but anisotropic variations in the refractive indices of n_o and n_e in the visible light region, and therefore, it produces measurable deviations between n_o and n_e, leading to the significant modulations of the phase-matching conditions for the backward- and forward-propagating E-mode phonon-polaritons. We note that the phonon-polariton softening observed at specific wavenumbers (i.e., $\omega_{3\,THz}$, $\omega_{4\,THz}$, and $\omega_{7\,THz}$) mainly originates from the temperature-dependent phase-matching conditions. Therefore, the anharmonic values calculated from the phonon-polariton frequency measured at a specific wavenumber could be either overestimated or underestimated.[29,36,39] However, since our single-shot pump-probe imaging spectroscopy is capable of observing not only the phonon-polariton frequencies but also the dispersion curves in a wide temperature range, we could determine the inherent anharmonic values of the transverse optical TO_1 and TO_3 modes without overestimating/underestimating their magnitude.

C. High damping rate of E-mode phonon-polaritons

Finally, we will discuss the high damping rate of phonon-polaritons caused by the bilinear coupling of either the TO_1 or the TO_3 mode to the relaxation mode.[17,18] Figures 8(a) and (b) show the temperature dependence of the observed damping rate for the three phonon-polariton components. For all the three components, the damping rate diminishes as the temperature decreases. The $\omega_{3\,THz}$ and $\omega_{4\,THz}$ components, originating from the same TO_1 mode but with different wavenumbers, have almost the same damping rate at 10 K. As the temperature increases, however, the $\omega_{4\,THz}$ component has a higher damping rate than the $\omega_{3\,THz}$ component. Even a larger temperature dependence was observed for the $\omega_{7\,THz}$ component belonging to the TO_3 mode; the damping rate at 375 K was three to four times greater than that at 10 K. Hence, the higher frequency component provides the higher damping rate at high temperatures. The following qualitative explanation accounts for these behaviors. The damping rate of the relaxation mode λ, which was experimentally estimated from the slope of the

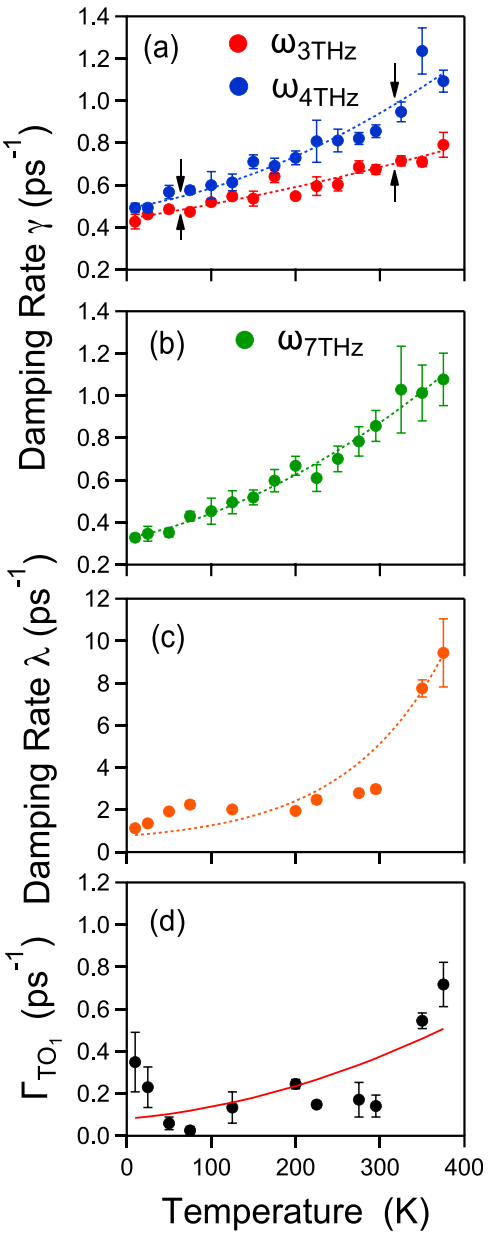

FIG. 8. Temperature dependence of the damping rates of LN components. (a) $\omega_{3\,THz}$ and $\omega_{4\,THz}$ components. (b) $\omega_{7\,THz}$ component. (c) The relaxation mode. (d) The pure TO_1 transverse optical mode. Arrows indicate the damping-rate difference of the $\omega_{3\,THz}$ and $\omega_{4\,THz}$ components at two exemplary temperatures. The broken lines are visual guides to the eye. A solid line traces the best fit calculated using Eq. (9). The parameter values used here appear in Table I.

electric response after $t = 0$,[17,18] increases with temperature, as shown in Fig. 8(c). In thermally assisted hopping among local potential energy minima, both the potential barrier and the frequency factor contribute to the damping rate. Because the structural phase transition takes place at 1483 K in LN,[2] we may assume that the configuration of the potential barrier hardly changes below 375 K. As a result, the variation of the damping rate is primarily determined by the frequency factor, that is, the phonon-polariton with a higher frequency component shows the higher damping rate at high temperatures.

In order to elucidate the above qualitative discussion, we used the same formalism successfully applied to $LiTaO_3$.[18] The wavenumber-dependent damping rate can be derived from the following equations of motion by considering the bilinear coupling of either the TO_1 or the TO_3 mode to the relaxation mode

$$\frac{d^2\boldsymbol{q}(t)}{dt^2} + \Gamma_{\mathrm{TO}_i}\frac{d\boldsymbol{q}(t)}{dt} + \omega_{\mathrm{TO}_i}^2\boldsymbol{q}(t) = A_{12}\boldsymbol{E}(t) + A_{1r}\boldsymbol{q}_r(t), \quad (6)$$

$$\frac{1}{\lambda(T)}\frac{d\boldsymbol{q}_r(t)}{dt} + \boldsymbol{q}_r(t) = A_{r1}\boldsymbol{q}(t), \quad (7)$$

$$\boldsymbol{p}(t) = A_{21}\boldsymbol{q}(t) + A_{22}\boldsymbol{E}(t). \quad (8)$$

Here, $\boldsymbol{q}(t)$ and $\boldsymbol{q}_r(t)$ are the coordinates for the vibration and relaxation modes, respectively, $\boldsymbol{E}(t)$ is the electric field, $\lambda(T)$ is the damping rate of the relaxation mode at a given temperature, $\boldsymbol{p}(t)$ is the polarization, and the A's are the coupling constants that satisfy $A_{12}A_{21} = \omega_{\mathrm{TO}_i}^2\varepsilon_0(\varepsilon_{st_i} - \varepsilon_{\mathrm{el}})$ and $A_{22} = \varepsilon_0(\varepsilon_{\mathrm{el}} - 1)$. Then, $A_{1r}A_{r1}$ is the coupling of either the TO_1 or the TO_3 mode to the relaxation mode, where ε_0 is the dielectric constant of vacuum. Also, ω_{TO_i} and Γ_{TO_i} are the natural frequency and decay rate of the pure transverse mode. The value of $\lambda(T)$ increased gradually with temperature from 1.1 ps^{-1} (10 K) to 9.4 ps^{-1} (375 K) as shown in Fig. 8(c). We note that without the bilinear coupling of the TO_i modes to the relaxation mode, the above formalism reduces to the simple equations of motion for damped harmonic oscillators, yielding the same phonon-polariton dispersions described in Eq. (3). We also stress that the bilinear coupling accounts for the high damping rate of phonon-polaritons, while it does not significantly contribute to the modulation of the phonon-polariton dispersion curves[17,18] and the phonon-polariton frequency shift discussed in Sec. III B. According to the calculation with adjustable parameters of Γ_{TO_1} and $A_{1r}A_{r1}$, we found that the parameter $A_{1r}A_{r1}$ was $(1.2 \pm 0.1)\times 10^4\,\mathrm{cm}^{-2}$ for the TO_1 mode in order to reproduce the wavenumber-dependent damping rate, whose value was independent of temperature because LN exhibited no structural phase transition in this temperature range. The obtained value is comparable with the value for $LiTaO_3$.[18] In the same manner, we roughly estimated that the value of $A_{1r}A_{r1}$ fell in the range of $3 \times 10^4\,\mathrm{cm}^{-2}$ to $6 \times 10^4\,\mathrm{cm}^{-2}$ for the TO_3 mode, which was three to five times larger than the value for the TO_1 mode. On the other hand, we found that the parameter Γ_{TO_1}, which was estimated separately from the bilinear coupling, depends on temperature as shown in Fig. 8(d). The damping rate at a given temperature can be generally expressed as

$$\Gamma(T) = \Gamma(0) + N_1\left\{1 + 2n\left(\frac{\omega(0)}{2}, T\right)\right\} + N_2\left\{1 + 3n\left(\frac{\omega(0)}{2}, T\right) + 3n^2\left(\frac{\omega(0)}{3}, T\right)\right\}, \quad (9)$$

where $\Gamma(0)$ and N_1 and N_2 are the damping rate at 0 K and the anharmonic constants attributed to the three- and four-phonon processes, respectively.[36,37] By applying Eq. (9) to Γ_{TO_1}, as shown by the solid curve in Fig. 8(d), we could roughly reproduce the temperature dependence of the decay rate for the pure transverse TO_1 mode using the parameter values of $\Gamma(0)$, N_1, and N_2 listed in Table I.

Figure 9 displays the observed damping rate of the TO_1 mode as a function of the wavenumber at different temperatures. All of the experimental data marked by the solid circles are fairly in good agreement with the theoretical calculation with the $A_{1r}A_{r1}$ parameter value of $(1.2 \pm 0.1) \times 10^4\,\mathrm{cm}^{-2}$ and the particular values of Γ_{TO_1}. The phonon-polariton with a higher frequency and wavenumber had a larger damping rate, particularly at high temperatures. The equations of motion presented in Eqs. (6)–(8) clearly describe how phonon-polaritons with a higher frequency factor can interact frequently with the relaxation mode through the bilinear coupling of $A_{1r}A_{r1}$. Because the relaxation mode is not fully activated at low temperatures, the damping rate of the TO_1 mode shows a small frequency dependence. On the other hand, as the temperature increases, the phonon-polariton with a higher frequency factor can display a larger damping rate through interactions with the thermally activated relaxation mode. The TO_3 mode showed that both a high frequency factor (~7 THz) and larger bilinear coupling ($3 \times 10^4\,\mathrm{cm}^{-2}$~$6 \times 10^4\,\mathrm{cm}^{-2}$) might be responsible for the high damping rate observed.

Finally, we provide a qualitative discussion of the role of the acoustic phonons and the relaxation mode with respect to the overall anharmonic behavior of the phonon-polaritons. The temperature dependence of ω_{TO_i} and Γ_{TO_1} has been

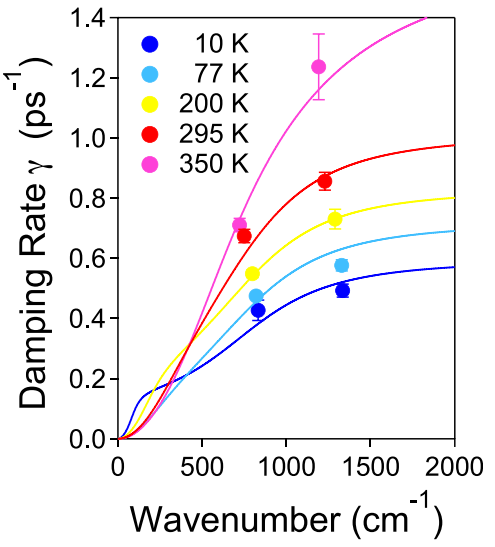

FIG. 9. Calculated damping rate of the TO_1 mode as a function of the wavenumber for various temperatures. The coupling constant of $A_{1r}A_{r1}$ in the range of $(1.2 \pm 0.1) \times 10^4\,\mathrm{cm}^{-2}$ was used to reproduce the experimental results.

analyzed using Eqs. (5) and (9) to estimate the anharmonicity arising from acoustic phonons. On the other hand, the use of Eqs. (6)–(8) reproduces the observed wavenumber dependence of γ for every temperature quite satisfactorily (see Fig. 9). Since both respective procedures explain the important parts of the experimental results, these two procedures must be indispensable to understanding the overall anharmonicity of ferroelectric phonon-polaritons. As shown in Fig. 8(c), the damping rate λ is relatively large and increases with temperature, implying that acoustic phonons play an important role in the thermal activation of the relaxation mode. Subsequently, the thermally activated relaxation mode contributes to the high damping rate of γ through the bilinear coupling mechanism, and the wavenumber dependence of γ is reasonably explained in Eqs. (6)–(8). Further works are needed to elucidate the contribution of acoustic phonons to the relaxation mode. However, the analysis presented here demonstrates that using our unique single-shot spectroscopy, we could discuss the overall anharmonic characteristics of the E-mode phonon-polaritons arising from both acoustic phonons and the relaxation mode.

IV. CONCLUSION

We have implemented single-shot pump-probe imaging spectroscopy with an echelon mirror to disclose the anharmonic phonon-polariton dynamics of ferroelectric LN in a wide temperature range from 10 K to 375 K. This method simultaneously eluded the photorefractive effects that persistently appear at low temperatures. We found that the anharmonicity arising from the three- and four-phonon processes introduces slight but anisotropic variations in the refractive indices of n_o and n_e in the visible light region. This variation then leads to the significant modulation of the phase-matching conditions for E-mode phonon-polaritons, which provides the main contribution to the observed temperature-dependent frequency shift. After subtracting the influence of the frequency shift due to the phase-matching conditions, we numerically described the temperature dependence of the frequency shift for E-mode phonon-polaritons. We also obtained the wavenumber dependence of the damping rate by analyzing the equations of motion which include the bilinear coupling of either the TO_1 or the TO_3 mode to the relaxation mode. The temperature-dependent decay rate of the TO_1 mode was then evaluated. We found that phonon-polaritons with higher frequencies and wavenumbers produce higher damping rates, in particular at high temperatures, by frequently interacting with the relaxation mode. We believe that these findings contribute to not only the fundamental understanding of anharmonic behaviors in ferroelectrics but also the future nonlinear THz applications of various ferroelectric materials.

ACKNOWLEDGMENTS

This work was supported in part by Grants-in-Aid for Scientific Research (Nos. JP16H04001, JP16H06010, JP16H03820, and JP16H06364) from JSPS and MEXT.

[1]Y. Xu, *Ferroelectric Materials and Their Applications* (North–Holland, Elsevier Amsterdam, 1991).
[2]A. S. Barker, Jr. and R. Loudon, Phys Rev. **158**, 433 (1967).
[3]H. Hirori, A. Doi, F. Blanchard, and K. Tanaka, Appl. Phys. Lett. **98**, 091106 (2011).
[4]A. G. Stepanov, J. Hebling, and J. Kuhl, Appl. Phys. Lett. **83**, 3000 (2003).
[5]J. A. Fülöp, L. Pálfalvi, S. Klingebiel, G. Almási, F. Krausz, S. Karsch, and J. Hebling, Opt. Lett. **37**, 557–559 (2012).
[6]S. W. Huang, E. Granados, W. R. Huang, K. H. Hong, L. E. Zapata, and F. X. Kärtner, Opt. Lett. **38**, 796 (2013).
[7]K. Takeya, T. Minami, H. Okano, S. R. Tripathi, and K. Kawase, APL Photonics **2**, 016102 (2017).
[8]C. Zhang, Y. Avetisyan, A. Glosser, I. Kawayama, H. Murakami, and M. Tonouchi, Opt. Express **20**, 8784 (2012).
[9]Y. Avestisyan, C. Zhang, I. Kawayama, H. Murakami, T. Somekawa, H. Chosrowjan, M. Fujita, and M. Tonouchi, Opt. Express **20**, 25752 (2012).
[10]C. Somma, K. Reimann, C. Flytzanis, T. Elsaesser, and M. Woemer, Phys. Rev. Lett. **112**, 146602 (2014).
[11]T. Kampfrath, K. Tanaka, and K. A. Nelson, Nat. Photonics **7**, 680 (2013).
[12]K. Yoshioka, Y. Minami, K. Shudo, T. D. Dao, T. Nagao, M. Kitajima, J. Takeda, and I. Katayama, Nano Lett. **15**, 1036 (2015).
[13]K. Yoshioka, I. Katayama, Y. Minami, M. Kitajima, S. Yoshida, H. Shigekawa, and J. Takeda, Nat. Photonics **10**, 762 (2016).
[14]I. Katayama, H. Aoki, J. Takeda, H. Shimosato, M. Ashida, R. Kinjo, I. Kawayama, M. Tonouchi, M. Nagai, and K. Tanaka, Phys. Rev. Lett. **108**, 097401 (2012).
[15]A. von Hoegen, R. Mankowsky, F. Fechner, M. Forst, and A. Cavalleri, Nature **555**, 79 (2018).
[16]K. Nakagawa, A. Iwasaki, Y. Oishi, R. Horisaki, A. Tsukamoto, A. Nakamura, K. Hirosawa, H. Liao, T. Ushida, K. Goda, F. Kannari, and I. Sakuma, Nat. Photonics **8**, 695 (2014).
[17]Y. Ikegaya, H. Sakaibara, Y. Minami, I. Katayama, and J. Takeda, Appl. Phys. Lett. **107**, 062901 (2015).
[18]G. P. Wiederreecht, T. P. Dougherty, L. Dhar, K. A. Nelson, D. E. Laird, and A. M. Weiner, Phys. Rev. B. **51**, 916 (1995).
[19]U. T. Schwarz and M. Maier, Phys. Rev. B **58**, 766 (1998).
[20]K. Buse, A. Adibi, and D. Psaltis, Nature **393**, 665 (1998).
[21]C. Barsi, W. Wan, and J. W. Fleischer, Nat. Photonics **3**, 211 (2009).
[22]Z. Xu, J. Gong, S. Xu, and Y. Xu, Solid State Commun. **152**, 473 (2012).
[23]I. Katayama, H. Sakaibara, and J. Takeda, Jpn. J. Appl. Phys., Part 1 **50**, 102701 (2011).
[24]Y. Minami, Y. Hayashi, J. Takeda, and I. Katayama, Appl. Phys. Lett. **103**, 051103 (2013).
[25]Y. Minami, H. Yamaki, I. Katayama, and J. Takeda, Appl. Phys. Express **7**, 022402 (2014).
[26]J. Takeda, W. Oba, Y. Minami, T. Saiki, and I. Katayama, Appl. Phys. Lett. **104**, 261903 (2014).
[27]Y. Minami, K. Horiuchi, K. Masuda, J. Takeda, and I. Katayama, Appl. Phys. Lett. **107**, 171104 (2015).
[28]P. G. Klemens, Phys. Rev. **148**, 845 (1966).
[29]M. Balkanski, R. F. Walls, and E. Haro, Phys. Rev. B **28**, 1928 (1983).
[30]Z. Su, Q. Meng, and B. Zhang, Opt. Mater. **60**, 443 (2016).
[31]Q. Meng, B. Zhang, S. Zhong, and L. Zhu, Appl. Phys. A **122**, 582 (2016).
[32]H. Sakaibara, Y. Ikegaya, I. Katayama, and J. Takeda, Opt. Lett. **37**, 1118 (2012).
[33]S. Margueron, A. Bartasyte, A. M. Glazer, E. Silmon, J. Hlinka, I. Gregora, and J. Gleize, J. Appl. Phys. **111**, 104105 (2012).
[34]S. Sanna, S. Neufeld, M. Rüsing, G. Berth, A. Zrenner, and W. G. Schmidt, Phys. Rev. B. **91**, 224302 (2015).
[35]W. D. Johnson, Jr. and I. P. Kaminow, Phys. Rev. **168**, 1045 (1968).
[36]J. F. Kong, W. Z. Shen, and Q. X. Guo, Phys. Status Solidi B **250**, 329 (2013).
[37]X. Xu, T.-C. Chong, S. Solanki, X. Liang, and S. Yuan, Opt. Mater. **26**, 489 (2004).
[38]A. Jayaraman and A. A. Ballman, J. Appl. Phys. **60**, 1208 (1986).
[39]N. Kokanyan, D. Chapron, and M. D. Fontana, Appl. Phys. A **117**, 1147 (2014).
[40]U. Schlarb and K. Betzler, Phys. Rev. B **48**, 15613 (1993).